ORIGINAL PAPER

Effects of an enhanced fibre–matrix adhesion on the fatigue behaviour of composite materials under very high cycle fatigue

M. Bartelt[1] · P. Horst[1] · S. Heimbs[1]

Abstract

The fatigue behaviour of two glass fibre-reinforced epoxy composite materials with a cross-ply layup is investigated in the very high cycle fatigue (VHCF) regime with up to 10^8 load cycles. In addition to the influence on the fatigue lifetime, different materials can also cause a different damage phenomenology. One reference fibre (OC111A) and one fibre with increased fibre–matrix adhesion (SE2020) are tested. The experimental and numerical investigations show that the damage threshold is shifted to higher loads with increased fibre–matrix adhesion, but the damage mode of delaminations becomes more important.

Keywords Composite materials · Very high cycle fatigue · Fatigue damage

1 Introduction

Extensive research of fatigue of fibre-reinforced plastics (FRP) is conducted since the 1960s to encounter the complexity of damage phenomenology. VHCF recently came into focus due to its importance in helicopter rotor blades, aircraft propellers and in wind power industry as rotor blades experience more then 10^8 load cycles during their lifetime [1, 2]. To enhance the understanding of fatigue mechanisms for an efficient design of rotor blade structures, the VHCF regime needs to undergo further investigation [3].

The first challenge in VHCF testing are long testing times as 10^8 load cycles at 3 Hz take 386 days. Reducing testing times using higher testing frequencies yields to hysteretic specimen heating [4] and the need for active cooling [5] or intermittent operation [6]. Other issues are the self-fatigue of testing equipment and fluctuations in test results. Therefore, special testing facilities and a broad database of testing results are necessary.

The available research concentrates on S–N curves with different parameter combinations, prediction models and fatigue limits. Few research studies cover detailed damage phenomenology. A comprehensive overview is given by

Shabani et al. [7], especially regarding test methods and damage mechanisms. Investigations of composite materials for wind turbine blades are conducted by Reed [8], Mandell et al. [9–11], Creed [12] and Sutherland [13].

Studies of Hosoi et al. [14–19] investigated basic damage phenomena such as crack and delamination propagation and the edge effect for cross-ply tension specimens up to 10^8 load cycles. First results on cross-ply and quasi-isotropic CFRP layups showed an edge effect by cracks mainly initiating at the edges and growing over the specimen width. Also, a change in damage phenomenology was observed when switching from high loads to low loads. At high loads, cracks grew first and after a significant crack density was reached, delamination growth started. For low loads, the crack and delamination growth started simultaneously. Also, the crack density was higher for high loads. This is explained by the delamination stopping growth of nearby cracks at low loads. Later work of Hosoi et al. [5, 20, 21] concentrates on the prediction of the first transversal crack initiation.

Cross-ply ($[90/0]_s$) and angle-ply ($[\pm 45]_s$) coupon specimens were tested by Adam et al. [22–24] under four-point bending with a frequency of 50 Hz and a stress ratio of R = − 1. Damage mechanisms, their interaction and stiffness degradation of the OC111A/RIM135 composite were investigated. For cross-ply specimens, with the inner 0°-ply acting to a certain amount as backing layer, transverse cracking was found to affect the stiffness predominantly and after crack saturation is reached, stiffness reduction slows down significantly. The supposed

✉ M. Bartelt
martin.bartelt@tu-braunschweig.de

1 TU Braunschweig, Institute of Aircraft Design
and Lightweight Structures, Hermann-Blenk-Str. 35,
38108 Braunschweig, Germany

transverse cracking threshold—in a sense the fatigue limit—was specified between 0.19% and 0.22% of the transverse strain.

As the development of materials is going on, the effects of changed material properties on the detailed fatigue behaviour, especially on the damage propagation, are still unknown. This paper examines the influence of the change of the glass fibre material from OC111A to SE2020 in a cross-ply layup, including their individual sizing. The matrix material RIM135/RIM137H, as well as the fibre volume content and the manufacturing process widely remain the same. This change in the fibre material is interesting since the new material is optimised for high fatigue performance and, therefore, particularly useful to investigate effects on the fatigue damage phenomenology and the question of the existence of a fatigue limit.

Data on OC111A were taken from former studies by Adam et al. [4, 22–26]. A special four-point bending test setup has been developed [25], which basically was used in the studies on SE2020 too. However, it has been enhanced in several ways, as described in the next section of this paper.

2 Experimental approach

Prior to the experimental results, the VHCF bending test rig, the material and specimen data, the conducted experiments and the damage evaluation are presented.

2.1 VHCF bending test rig

The basic principle of the VHCF test rig (Fig. 1) widely follows the one presented by Adam and Horst [25], but several features are new. As before, it contains a total of four parallel test setups, mounted on a damping concrete base. On every test setup, the specimen is clamped in a four-point bending device with a lightweight centre bearing and two fixed outer bearings, which are connected through two loadcells to the base plate. The centre bearing is deflected by an electrodynamic actuator and contains an LED-screen to provide light for the high-resolution camera to record the microcracks and delamination.

The camera is now integrated in the computer-controlled system of the test rig. The test stops automatically and a picture is taken at predefined load cycle numbers. Also new is the individual observation of the specimen surface temperature by a small thermal camera-sensor. The temperature data are recorded and if the mean surface temperature rises above 25°C the test stops automatically. Also, the two fans for cooling the specimens are controlled through temperature data. Furthermore, environmental temperature and humidity are recorded. The complete system is encapsulated by a thermal, sound insulating and air-conditioned housing, keeping constant 20°C ambient temperature. The VHCF test rig is working at frequencies from 20 Hz to 80 Hz.

The distance between the inner and outer bearings is $l_L = 40\,mm$ and $l_P = 80\,mm$ as shown in Fig. 2. Since there is a constant bending moment between the inner

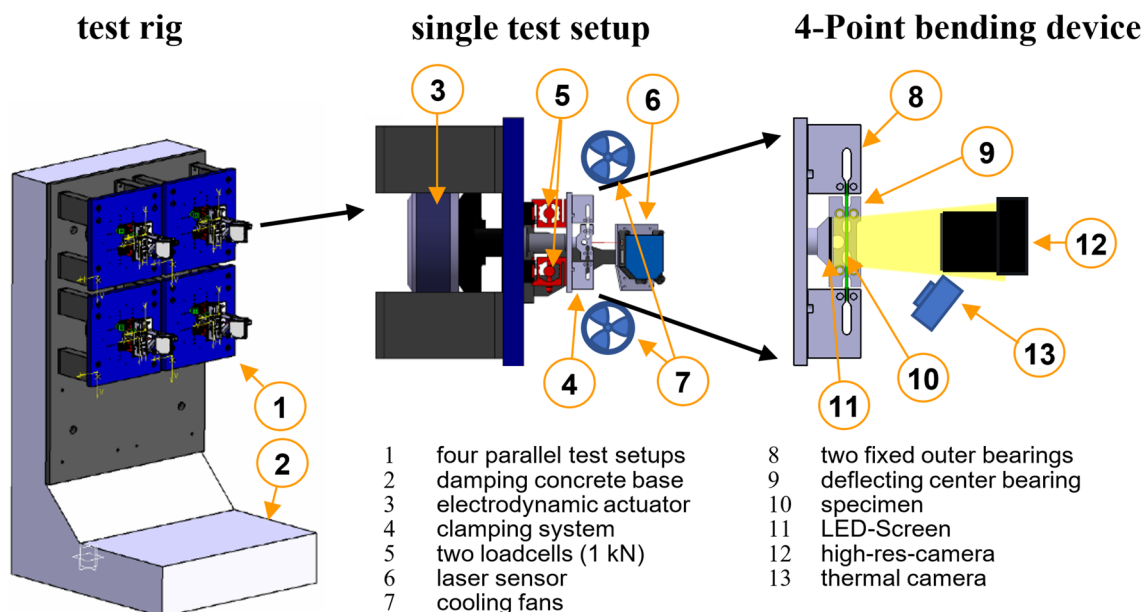**Fig. 1** VHCF bending test rig based on the setup by Adam [24]

test rig — single test setup — 4-Point bending device

1 four parallel test setups
2 damping concrete base
3 electrodynamic actuator
4 clamping system
5 two loadcells (1 kN)
6 laser sensor
7 cooling fans

8 two fixed outer bearings
9 deflecting center bearing
10 specimen
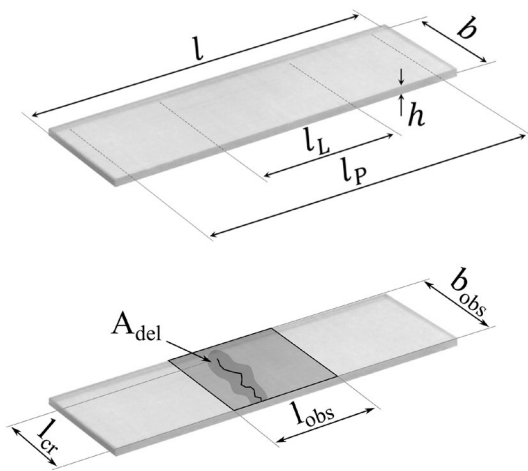11 LED-Screen
12 high-res-camera
13 thermal camera

Fig. 2 Geometric parameters according to [4]

Table 1 Mechanical properties of the glass fibres

Mech properties	Unit	OC111A [27]	SE2020 [28]
E_{11}	GPa	80.7	81
R_{11}	MPa	2560	2200–2500
ρ	g/cm^3	2.58	2.62

Table 2 Tensile mechanical properties of the UD-laminates

Mech. properties	Unit	OC111A/RIM135 [24]	SE2020/ RIM135 [29]
E_{11}	GPa	36.5	33.8
E_{22}	GPa	7.5	7.8
R_{11}	MPa	806	744
R_{22}	MPa	27	60
ϵ_{11}	%	2.3	2.33
ϵ_{22}	%	0.34	1.1
ϕ_f	%	41.7	39.7
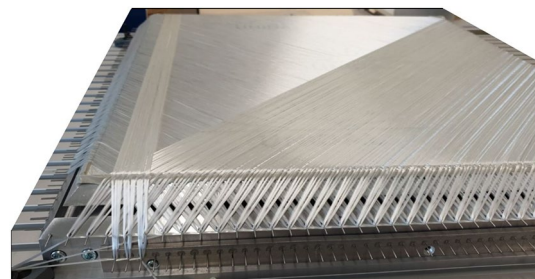
Fig. 3 Unsewn laminate fabrication via CNC roving stacking

bearings under four-point bending, there is a particularly large testing and evaluation area compared to three-point bending.

2.2 Materials and specimens

As mentioned above, the OC111A fibre (produced by *Owens Corning*) used by Adam et al. [24] for their tests is replaced with a more modern VHCF-optimised SE2020 fibre from *3B-Fibreglass*. The mechanical properties of the glass fibres are very similar (see Table 1).

The mechanical properties of the UD-laminates are listed in Table 2. For the SE2020/RIM135 composite, they were obtained in a material characterisation by Chen [29].

The SE2020 roving is optimised for fatigue by a special sizing, according to the manufacturer's brochure. This effect is also visible by the comparison of the tensile transverse strength R_{22} of the composite materials, where the strength of the composite with the SE2020 roving is 122% higher. Therefore, the sizing enhances the fibre–matrix interface.

For the OC111A test series, a $[90/0]_s$ layup with a 1200 tex roving, a ply thickness of 0.5 mm and a fibre volume content of 42 % is used. To manufacture the same ply thickness with the 600 tex SE2020 roving, the layers are stacked twice. This results in a comparable $[90_2/0_2]_s$ layup.

The cross-ply laminates reduce interaction between the layers compared to quasi-isotropic layups. This is helpful in identifying the actual effects of the material.

The layups of the base laminates are produced by CNC roving stacking as shown in Fig. 3. To gain high-quality surfaces and a minimum of disturbances, the RTM process is then used with the epoxy system Momentive RIMR135R/ RIMH137H, similar to Adam et al. [24].

The edges of the specimens are grinded and polished to prevent additional crack initiation due to notches or imperfections.

With an average fibre volume fraction of 39.7%, the composite already provides a high fatigue resistance. The specimens have a length of $l = 82\,mm$, a width of $b = 25\,mm$ and a thickness of $h = 2\,mm$ as shown in Fig. 2.

In an additional characterisation, the surface strain to first crack $\epsilon_{22,c}^{90°}$ under quasi-static four-point bending for the $[90_2/0_2]_s$ layup of the SE2020/RIM135 composite is determined. With 1.6% compared to 0.43% [24] of the $[90/0]_s$ layup with the OC111A fibre, the improvement is huge and can be directly traced back to the higher transverse strength and the improved fibre–matrix interface.

2.3 Conducted experiments

Cross-ply laminates with a $[90_2/0_2]_s$ layup are tested with the same load levels as Adam et al. [24] used, to sustain comparability. Load levels 1, 2 and 5 are added to gather more data under high loads or in the area of low crack initiation for the SE2020 specimens. The load levels are defined by the surface strain and are shown in Table 3 with the number of tested specimens for both materials. Tests are conducted until no more damage development can be expected or 10^8 load cycles are reached.

Surely, for the high load levels 1 and 2, the real fatigue range belongs more to the HCF than VHCF range, but they are needed to compare the phenomena as well as to relate them to the VHCF results.

2.4 Damage evaluation

To sustain comparability, all parameters used for damage evaluation are calculated as in Adam et al. [3]. The simplified four-point bending flexural modulus is expressed by

$$\bar{E}_{\text{xb}} = \frac{\hat{F}}{\hat{w}_{\text{max}}} \frac{(l_{\text{P}} - l_{\text{L}})}{bh^3} \left(\frac{1}{4}(l_{\text{P}} - l_{\text{L}})^2 + \frac{3}{4}l_{\text{L}}(l_{\text{P}} - l_{\text{L}}) + \frac{3}{8}l_{\text{L}}^2 \right) \tag{1}$$

with the force amplitude $\hat{F}$, deflection amplitude $\hat{w}_{\text{max}}$, load bearing distance l_L, test area length l_P, the width b and the thickness h of the specimen. The crack density

$$\rho = \frac{\sum_{i=0}^{n_{\text{R}}} l_{\text{R},i}}{b_{\text{obs}} l_{\text{obs}}} \tag{2}$$

is calculated by the sum of all crack lengths $l_{R,i}$ divided by the observation area $b_{obs} \cdot l_{obs}$. Likewise, the delamination area ratio

$$H_{\text{del}} = \frac{A_{\text{del}}}{b_{\text{obs}} l_{\text{obs}}} \tag{3}$$

is calculated by the delamination area A_{del} divided by the observation area. As front- and back-side cracks are counted, the total crack length is divided by twice the observation area. This also applies to the calculation of the delamination. The geometric parameters are shown in Fig. 2.

An automated procedure has been developed to detect the parameters needed to calculate ρ and H_{del}. Cracks are counted and the delamination area is determined by a Python code using the OpenCV library. In every test, a minimum of 100 photos are automatically taken.

For crack and delamination detection, the total specimen width ($b = b_{obs}$) and a length of $l_{obs} = 28\,mm$ between the two inner bearings is used (see Fig. 2).

For high crack densities, the chance of a front side crack covering a back-side crack rises. It is not possible to detect the back-side crack on a photo manually or by the crack detection software. Also, delamination areas from the back side and the front side cannot be distinguished if they overlap. These high crack densities and delamination area ratios normally only occur at HCF tests, so the detection software detects cracks and delaminations for VHCF specimens with typically low damage accumulations with a high accuracy. The developed software is successfully validated by comparing results with manually measured data.

2.4.1 Crack and delamination evaluation model

A parametric finite-element (FE) model is developed using ANSYS® and its parametric design language (APDL) to support the understanding of the process of crack and delamination development. As shown in Fig. 4A, the model consists of the entire specimen under four-point bending with the deflection boundary conditions depicted as bearings and the applied force as arrows. The model is able to simulate a variable number of cracks in the outer layer and delaminations with adjustable size growing from the crack tips along the layer interface. This enables parametric studies with different crack densities and delamination area ratios under quasi-static loading.

Figure 4B shows the $[90_2/0_2]_s$ layup and the meshing in a close-up view at the centre crack. The use of Solid 186 and Solid 187 elements enables the model to calculate valid stresses and stress intensity factors in the vicinity of the crack or delamination tip. The model width is reduced from 25 mm to 4 mm to lower the calculation time without significant differences in results.

To show the opening of the crack and the delamination, a typical displacement-plot in thickness direction (Z)

Table 3 Load levels surface strain number of specimens of the VHCF tests series

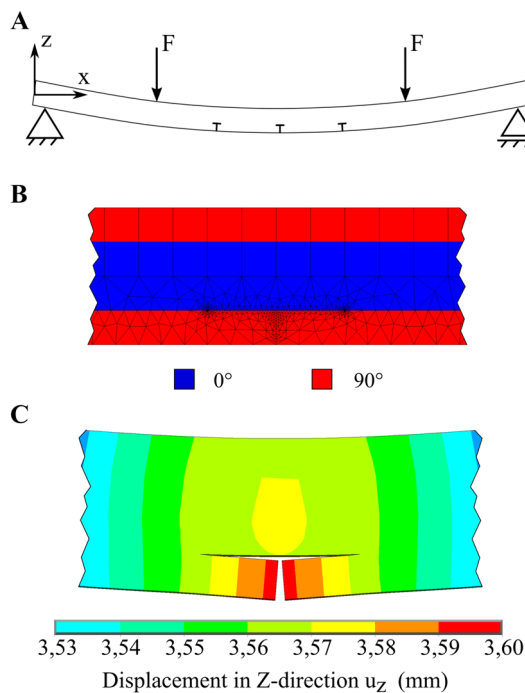| Load level	Surface strain	Number of specimens	
	$\epsilon_{22,0}^{90°}$ (%)	OC111A [23]	SE2020
1	0.68		2
2	0.55		2
3	0.43	2	4
4	0.36	2	4
5	0.3		4
6	0.25	12	4
7	0.22	2	3
8	0.19	4	
9	0.13	4	

Fig. 4 Overview FEM-model: **A** four-point bending with three cracks with delamination; **B** close-up view at centre crack of mesh and layup; **C** close-up displacement-plot at centre crack

around the centre crack is shown in Fig. 4C. The model is validated by comparison to analytical results (single crack in homogeneous material).

3 Influence of glass fibre material

The evaluation and presentation of the test results from two test series with several load levels and several specimens per load level with different types of damage is not simple. Therefore, first, an overview of the fatigue damages in the observation area for both test series with one exemplary photograph per load level is given in Fig. 5.

Visible damages are transverse cracks in the 90°-layers and delaminations starting from the cracktip at the interface to the adjacent 0°-layer and growing along this interface in longitudinal direction. Due to the swelling loads ($R = -1$) in the tests, the damages occur on the back and front side of the specimens, but they are hard to distinguish.

To determine the influence of the enhanced fibre–matrix interface under VHCF in detail, the following aspects are investigated. A transverse cracking threshold is defined, the crack paths are examined under the microscope, the crack initiation positions are evaluated concerning an edge effect and the flexural modulus degradation as well as the crack density and delamination area ratio are compared. Using the FE model, phenomenological findings are confirmed.

3.1 Transverse cracking threshold

As fatigue damage decreases with the fatigue load, a damage threshold is assumed at a certain load. As for the OC111A test series for every load level cracks occurred, Adam et al. [23] defined a transverse cracking threshold between weak area cracking and the occurrence of a regular crack pattern. They specify the cracks of load levels 8 and 9 as weak area cracks because of the scattered crack growth as it can be seen in Fig. 5. For load level 7 and higher, they see the commonly known regular crack pattern of cross-ply
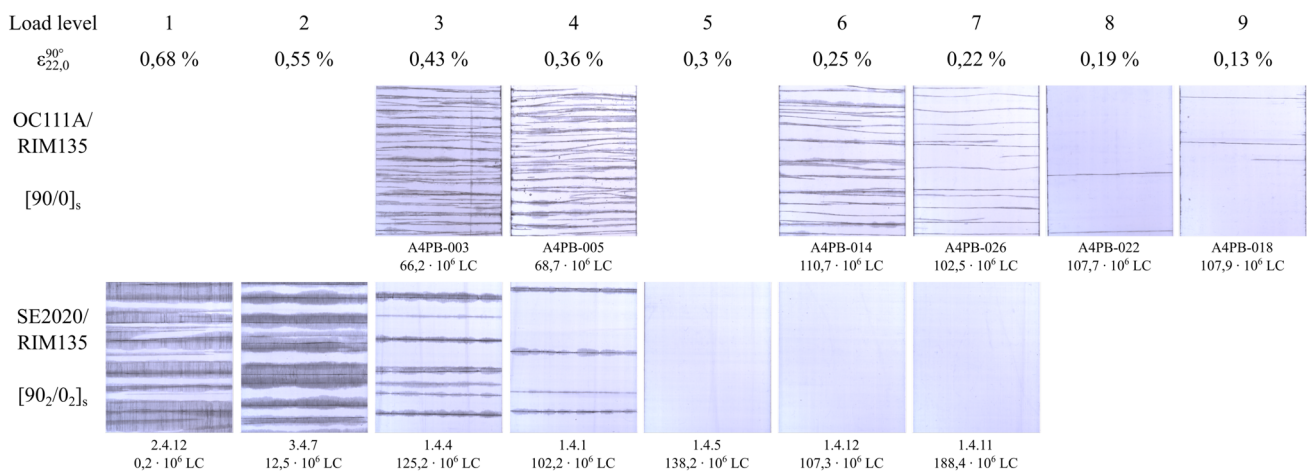

Load level	1	2	3	4	5	6	7	8	9
$\varepsilon_{22,0}^{90°}$	0,68 %	0,55 %	0,43 %	0,36 %	0,3 %	0,25 %	0,22 %	0,19 %	0,13 %
OC111A/ RIM135 [90/0]$_s$			A4PB-003 66,2 · 10⁶ LC	A4PB-005 68,7 · 10⁶ LC		A4PB-014 110,7 · 10⁶ LC	A4PB-026 102,5 · 10⁶ LC	A4PB-022 107,7 · 10⁶ LC	A4PB-018 107,9 · 10⁶ LC
SE2020/ RIM135 [90$_2$/0$_2$]$_s$	2.4.12 0,2 · 10⁶ LC	3.4.7 12,5 · 10⁶ LC	1.4.4 125,2 · 10⁶ LC	1.4.1 102,2 · 10⁶ LC	1.4.5 138,2 · 10⁶ LC	1.4.12 107,3 · 10⁶ LC	1.4.11 188,4 · 10⁶ LC		

Fig. 5 Overview of fatigue damage of the two VHCF test series, one characteristic specimen of every load level at fatigue test end

specimens. Therefore, they specify the transverse cracking threshold between 0.19% (L8) and 0.22% (L7) of transverse surface strain for the OC111A/RIM135 composite.

Using the same definition for the SE2020-test series, the threshold can be expected around 0.43% (L4) of transverse surface strain. As there are also load levels with no cracks at all, a weak area cracking threshold may also be specified. This threshold is assumed at around 0.3% (L5) of transverse surface strain, noting that one single crack occurred in one specimen out of four from load level 5.

3.2 Crack paths

With respect to the improved fibre–matrix adhesion, it might be interesting to see, if the crack grows through the matrix or as commonly observed along the fibre–matrix interface.

Therefore, the edges of several fatigue-tested specimens were examined under the microscope. Microscopic photos of two exemplary specimens are shown in Fig. 6. The left photographs show the crack passing through the total 90°-layer in thickness direction and the delamination at the layer interface. The right ones show a close-up view of the crack path. The specimens are bent in the moment of the recording to open the crack and to make the crack path visible.

Inspecting the crack paths, it becomes obvious that for both composites the crack grows along the fibre–matrix interface and always jumps to the closest fibre. This indicates that the lowest crack resistance is provided by the

fibre–matrix interface, even for the improved interface of the SE2020 roving.

3.3 Edge effect

Due to transverse contraction effects, the stresses at the specimen edges are slightly enlarged, which leads to more crack initiations at the edges. Also, small previous damages or imperfections at the specimen sides can be the origin of edge initiations.

Thanks to the newly integrated automatic photography system in the VHCF test rig, the quite short moment of crack initiation is documented at most of the times. This enables an examination of the initiation sites and thus of the edge effect. For this purpose, the crack initiations are counted in a centred 15 mm wide area and two 5 mm wide edge areas. This means, if the crack initiations are distributed normally, 40% initiate in the edge areas and 60% in the centre area.

For the improved composite, the evaluation shows 50.4% of the cracks initiate in the 5 mm edge area. Therefore, it can be stated that there is a slight edge effect, with 10.4% more cracks in the edge areas, compared to the normal distribution.

Adam et al. [22] mention for the OC111A/RIM135 composite cracks mainly initiate at the free edge.

This could be considered as a lower edge effect for the improved material.

3.4 Fatigue degradation and damage evolution

For cross-ply laminates under four-point bending fatigue, the flexural modulus degradation, the crack density and the delamination area ratio are essential parameters to investigate the fatigue behaviour quantitatively. Since
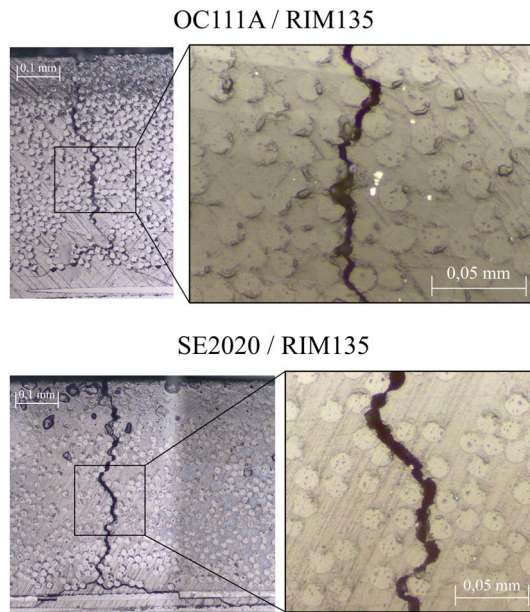

Fig. 6 Exemplary microscopic photograph of crack paths in the outer 90°-layer: (left) total crack and delamination at the layer interface; (right) close-up view at the crack path
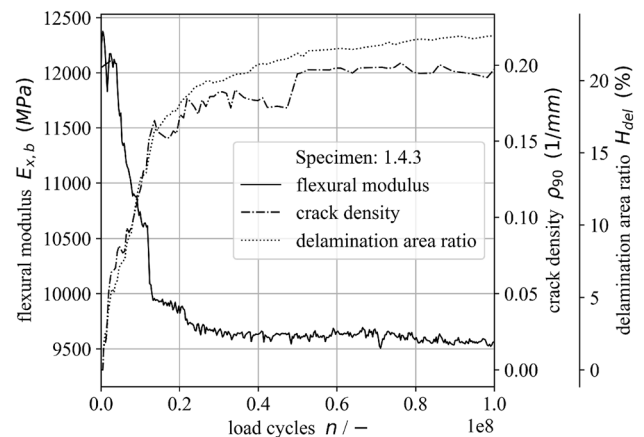

Fig. 7 Evolution of the smoothed flexural modulus, crack density and delamination area ratio over load cycles for specimen 1.4.3 of SE2020/RIM135 test series under load level 3

the degradation of the flexural modulus and the damage parameters crack density and delamination area ratio belong together, it is useful to look at these in parallel.

The evolution of these fatigue parameters over 10^8 load cycles is shown in Fig. 7 for an exemplary specimen of the SE2020-test series of load level 3.

From the diagram, it can be directly observed that these parameters match inversely very well. As the crack density and the delamination area ratio are rising, the flexural modulus is decreasing.

To make these data comparable between the two test series, the single specimen data of every load level are averaged. The flexural modulus is normalised with the initial flexural modulus of the undamaged specimen ($E_{x,b}/E_{x,b,0}$). These data are shown in Fig. 8, with the diagrams on the left side for the reference fibre and on the right side for the improved fibre. Also the standard deviation is given as grey area around the curves.

Since the specimens of load levels 1 and 2 developed damages very fast, the tests were stopped at low load cycles. Due to the high damage parameters reached in these tests, the detection precision of the damage parameters is low.

This means these tests are classified more in the HCF as in the VHCF range and thus, they are not listed in the diagram of Fig. 8.

The curves correlate with the first impression of the damages at the specimen photos in Fig. 5. This means they show a decreasing flexural modulus and increasing crack density and delamination area ratio for increasing load levels.

Only load level 3 of the OC111A/RIM135 composite shows less degradation than load level 4. This may be due to the small number of two specimens tested and the high scatter of the testing data, depending on measurement accuracy and specimen quality.

The degradation and damage growth reach a saturation after a while.

Comparing the two materials, the quantified parameters show less degradation of flexural modulus and a lower crack density for the SE2020 material. The delamination area ratio is nearly the same at least for load level 3.

The sudden rise of the flexural modulus of the SE2020/RIM135 composite at load level 3 around $0.88 \cdot 10^8$ load cycles is based on the premature test end of one strongly degraded specimen.
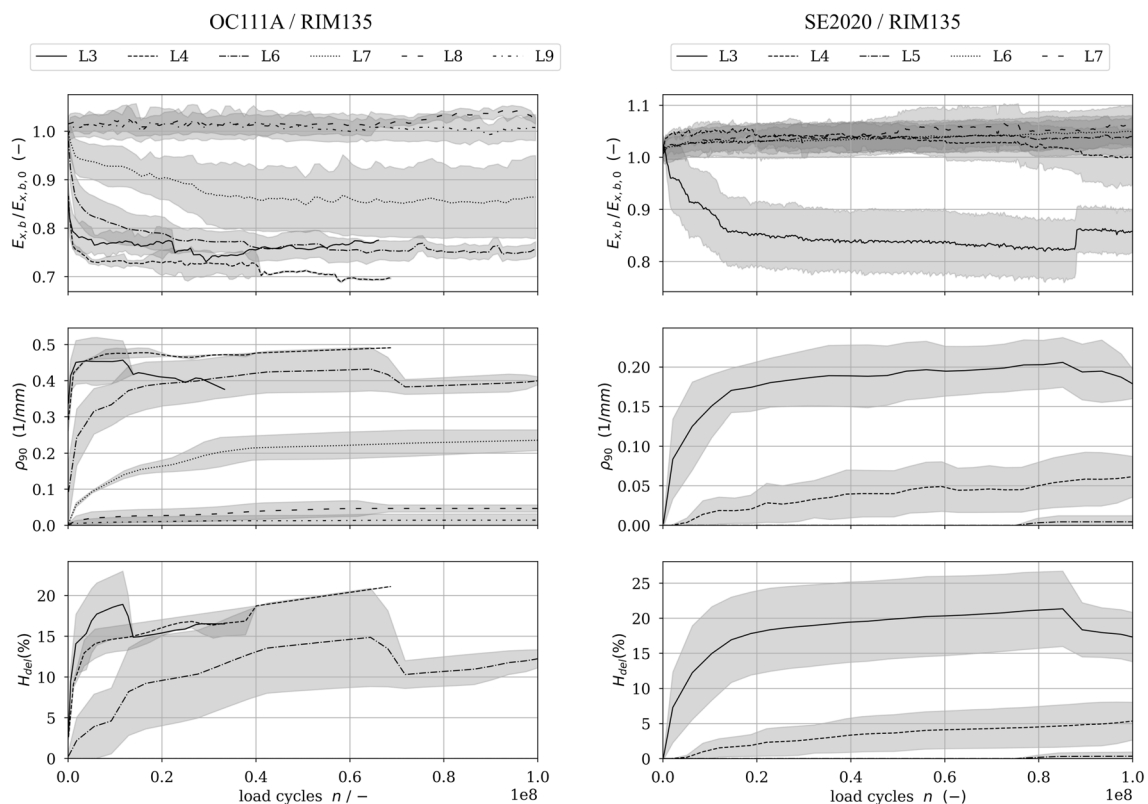

Fig. 8 Development of the flexural modulus, the crack density and the delamination area ratio of the two VHCF test series, averaged and smoothed over the samples of each load level, with specified standard deviation

The flexural modulus of the load levels 6 and 7 is also rising, but rather slowly and steady over the total test time. This rise is confirmed by very precise static bending tests before and after the VHCF test, where the specimens gained about 2.4%, respectively, 3.7% of the initial flexural modulus in average. This effect is astonishing. An explanatory approach might be the alignment of fibres in the zero-degree direction under load.

3.5 Change in damage phenomenology

Comparing the two test series in Fig. 5 again, in addition to the increased cracking threshold a change in damage phenomenology can be seen. While the OC111A/RIM135 composite develops many cracks with a lot of small delaminations, the SE2020 material develops fewer cracks with larger single delamination areas.

The data in Fig. 8 support this, as a lower crack density combined with nearly the same delaminations at load level 3 result in larger single delamination areas per crack.

To confirm this change in phenomenology, the delamination area per crack is shown in Fig. 9, for the load levels with damages.

Specimens of the OC111A composite reach a maximum delamination area per crack of $11\,mm^2$, compared to 15–$26\,mm^2$ for the improved material.

This leads to the following theory:

The improved fibre–matrix adhesion of the SE2020 fibre and its sizing leads to an enhanced transverse strength. This represents the decisive strength criterion for the outer 90°-ply under four-point bending and results in increased strain to first crack (see Sect. 2.2) as well as delayed crack initiation and slower crack growth under fatigue loads. The delamination resistance does not benefit as much as the cracking resistance from the enhanced fibre–matrix adhesion. As a result, more load cycles are available for delamination growth before a nearby transverse crack initiates, grows across the specimen width and stops the delamination growth.
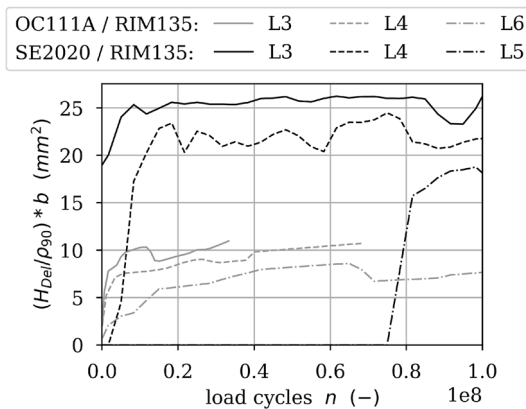
To prove this, the influence of the crack density on the delamination growth is investigated using the FE model described in Sect. 2.4.

3.6 Influence of the crack density on the delamination growth

The delamination growth is directly related to the stress intensity factor at the crack tip. To determine the influence of crack density, the stress intensity factors are calculated for the three models shown in Fig. 10 (only relevant model regions are shown). The model in (A) with one single crack serves as a reference for $\rho_{90} \approx 0\,mm^{-1}$. Model (B) and (C) simulate the crack densities $\rho_{90} = 0.2\,mm^{-1}$ and $\rho_{90} = 0.5\,mm^{-1}$ with three cracks, where the stress intensity factors are calculated at the tip of the centre crack.

The crack densities are chosen from the maximum densities reached by the materials under load level 3 (see Fig. 8).

The results of the FE calculations for load level 3 are listed in Table 4. In addition, to the modes I, II and III, the equivalent stress intensity factor K_V is calculated via
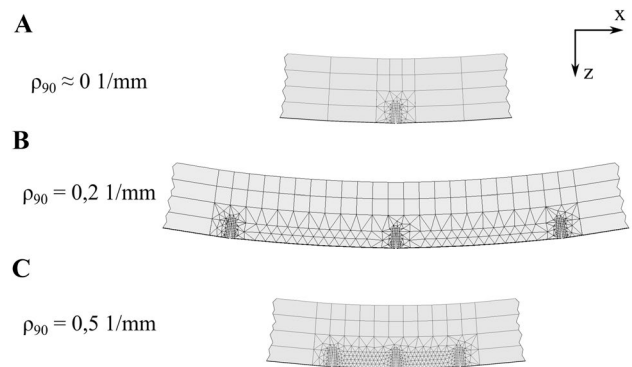

Fig. 10 FE models with one single crack as reference (**A**), three cracks with 5 mm distance (**B**) and three cracks with 2 mm distance (**C**) (only relevant model regions are shown)

Fig. 9 Delamination area per full width (25 mm) crack

Table 4 Stress intensity factors on tip of centre crack for different crack densities under load level 3 calculated by FEM

ρ_{90} (1/mm)	$K_I / \left(\frac{N}{\sqrt{mm^3}}\right)$	$K_{II} / \left(\frac{N}{\sqrt{mm^3}}\right)$	$K_{III} / \left(\frac{N}{\sqrt{mm^3}}\right)$	$K_V / \left(\frac{N}{\sqrt{mm^3}}\right)$
≈ 0	15.78	35.78	0.10	49.97
0.2	15.72	36.13	0.06	50.33
0.5	14.26	33.53	0.07	46.49

$$K_{\mathrm{V}} = \frac{K_I}{2} + \frac{1}{2}\sqrt{K_I^2 + 5{,}336 K_{II}^2 + 4 K_{III}^2}. \tag{4}$$

This equation is developed by Richard and Sander [30] for mixed-mode three-dimensional stress.

The results show a high mode II and a nearly-zero mode III stress intensity factor for all three crack densities under four-point bending.

The influence of a crack density of 0.2 $1/mm$ compared to the reference is negligible, but the influence of a high crack density of 0.5 $1/mm$ shows a 7.6% lower equivalent stress intensity factor.

This reduction is significant, because even small differences in load can have a huge impact on damage growth in the VHCF regime.

After confirming the influence of crack density on delamination growth, the subsequent vice versa question of influence of delamination on the crack initiation and growth is raised.

This means if the delamination lowers the crack initiation and growth, the already proven effect of higher delamination growth under lower or delayed crack initiation is self-amplifying and the sequence of events must be considered even more when assessing fatigue strength and developing fatigue prediction models.

3.7 Influence of the delamination on the crack initiation and growth

To determine the tendency to crack initiation, the surface strain $\sigma_{22}^{90°}$ between two cracks under load level 3 is calculated, as it is schematically shown in Fig. 11. Several FE calculations with delamination lengths (l_{del}) from 0 to 1.5 mm are conducted, and the resulting surface strain is plotted into the diagram of Fig. 11.
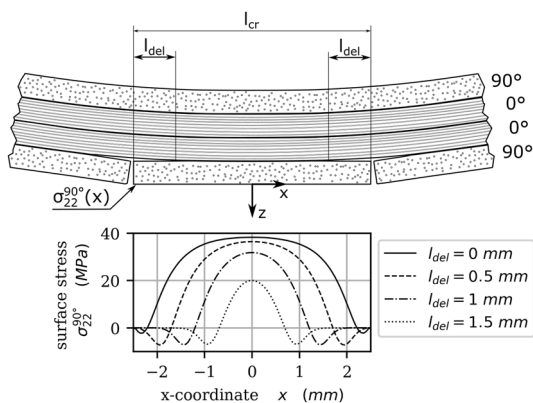
The diagram shows for a delamination length of 0 mm, a relatively wide centred area close to the reference surface strain of the undisturbed specimen of 40 MPa of load level 3. With increasing delamination length, the curve of surface stress decreases to about 50% of the reference stress for a delamination length of 1.5 mm.

Therefore, the influence of the delamination on the surface strain between two cracks and thus the crack initiation can be rated as quite strong. This confirms the self-amplification of the effect of delayed crack initiation leading to accelerated delamination growth.

As the calculations and assumptions made in this paper are idealised, an example of the fatigue damage behaviour in a realistic testing environment is shown in Fig. 12 to demonstrate the strong interactions between fatigue damages.

The figure shows a full width crack developing delaminations and a second crack initiating in the centre of the specimen right under the first crack. The first visible interaction is the slowdown of delamination growth between the two cracks. Then the second crack grows into the large delamination on the left side and is stopped by this delamination. A third crack initiates and grows over the full width. The delaminations from this third crack keep an exact distance to the delaminations of the second crack.

This example shows that the damage development is very complex and also strongly depends on parameters like the material strength distribution.

4 Conclusions

The influence of a strongly improved fibre–matrix adhesion of the fatigue optimised SE2020 glass fibre under VHCF is investigated by comparing it to a reference fibre from tests of Adam et al. [4, 23, 24, 26]. Extensive quasi-static and fatigue
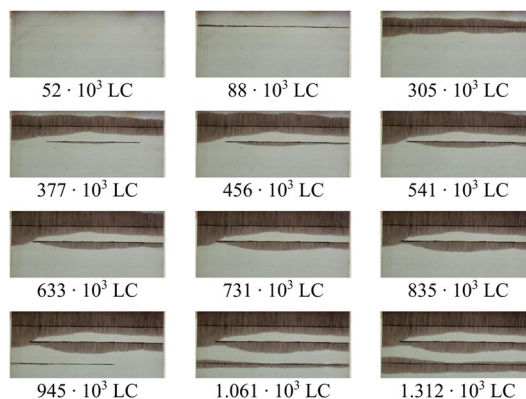
Fig. 11 Development of the surface stress between to cracks with a distance of 5 mm for different lengths of delaminations

Fig. 12 Example of damage interactions between cracks and delaminations

tests with several load levels are conducted and evaluated. The quasi-static tests from Adam [24] and Chen [29] show a significantly higher transverse strength and surface strain to first crack for the improved fibre material. First, evaluations of the fatigue test data show a shift of the transverse cracking threshold towards higher loads and a slightly lower edge effect. In the assessment of the crack paths, no differences are found between the composites.

A detailed view on the fatigue data reveals a change in damage phenomenology from high crack densities with a lot of small single delamination areas for the reference material to small crack densities and large single delamination areas for the improved material. This is proven by calculating the delamination area per full width crack for the relevant load levels and plotting it over 10^8 load cycles.

The reason for this is expected to be the delayed transverse crack initiation and slower crack growth due to the higher transverse strength and that the delamination resistance does not benefit as much from the enhanced fibre–matrix adhesion.

This leads to more time for delamination growth before it is stopped by a transverse crack.

To prove this, the influence of the crack density on delamination growth and vice versa are investigated, using parametric FE simulation studies.

The studies show a higher tendency towards delamination due to higher stress intensity factors at the crack tip for low crack densities. Further studies show a lower tendency towards crack initiation and growth due to lower surface strain between cracks for larger delaminations.

This is rated as a self-amplifying effect.

In general, it can be stated, that the improved fibre–matrix adhesion of the SE2020/RIM135 laminate leads to lower crack densities, less degradation and a higher transverse cracking threshold. In an evaluation of the fatigue behaviour of such an improved material, it is strongly suggested to be aware of the phenomenology change towards large single delamination areas. These cannot only contribute to a higher degradation of mechanical properties, but also to a stronger exposure to environmental dangers.

Declarations

References

1. Mandell, J.F., Samborsky, D.D.: DOE/MSU composite material fatigue database: Test methods, materials and analysis. Contractor Report SAND97-3002, Montana State University, (1997). https://doi.org/10.2172/578635
2. Marin, J.C., Barroso, A., Paris, F., Canas, J.: Study of fatigue damage in wind turbine blades. Eng. Fail. Anal. **16**(2), 565–668 (2009). https://doi.org/10.1016/j.engfailanal.2008.02.005
3. Bathias, C.: An engineering point of view about fatigue of polymer matrix composite materials. Int. J. Fatigue **28**, 1094–1099 (2006). https://doi.org/10.1016/j.ijfatigue.2006.02.008
4. Adam, T.J., Horst, P.: Fatigue damage and fatigue limits of a gfrp angle-ply laminate tested under very high cycle fatigue loading. Int. J. Fatigue **99**, 202–214 (2017). https://doi.org/10.1016/j.ijfatigue.2017.01.045
5. Hosoi, A., Suzuki, T., Kosugi, K., Atsumi, T., Shimamura, Y., Tsuda, T., Kawada, H.: Very high-cycle fatigue characteristics of cross-ply cfrp laminates in transverse crack initiation. In: International Committee on Aeronautical Fatigue, ICAF:838–846, (2019). https://doi.org/10.1007/978-3-030-21503-3_66
6. Weibel, D.O., Balle, F., Backe, D.: Ultrasonic fatigue of cfrp - experimental principle, damage analysis and very high cycle fatigue properties. Key Eng. Mater. **742**, 621–628 (2017). https://doi.org/10.4028/www.scientific.net/KEM.742.621
7. Shabani, P., Taheri-Behrooz, F., Samareh-Mousavi, S.S., Shokrieh, M.M.: Very high cycle and gigacycle fatigue of fiber-reinforced composites: a review on experimental approaches and fatigue damage mechanisms. Prog. Mater. Sci. **118**, 100762 (2021). https://doi.org/10.1016/j.pmatsci.2020.100762
8. Reed, R.M.: Long term fatigue of fiber reinforced composite materials for wind turbine blades. Master's thesis, Montana State University, (1991)
9. Mandell, J.F., Reed, R.M., Samborsky, D.D.: Fatigue of fiberglass wind turbine blade materials. Contractor Report SAND92-7005, Montana State University, (1992)
10. Mandell, J.F., Creed, R.F., Pan, Q., Combs, D.W., Shrinivas, M.: Fatigue of fiberglass generic materials and substructures. Wind Energy, ASME SED **15**, 207–213 (1994)
11. Mandell, J.F., Samborsky, D.D., Wang, L., Wahl, N.K.: New fatigue data for wind turbine blade materials. Technical Report AIAA-2003-0692, Montana State University, (2003). https://doi.org/10.1115/1.1624089

12. Creed, R.F.: High cycle tensile fatigue of unidirectional fiberglass composite tested at high frequency. Master's thesis, Montana State University (1993)

13. Sutherland, H.J., Mandell, J.F.: Application of the U.S. high cycle fatigue data base to wind turbine blade lifetime predictions. Proceeding of Energy Week, ASME:191–198, (1996)

14. Hosoi, A., Yagi, S., Nagata, K., Kawada, H.: Interaction between transverse cracks and edge delamination considering free-edge effects in composite laminates. In: Proceedings of the 16th International conference on composite materials (2007)

15. Hosoi, A., Arao, Y., Karasawa, H., Kawada, H.: High-cycle fatigue characteristics of quasi-isotropic cfrp laminates. Adv. Compos. Mater. **16**(2), 151–166 (2007). https://doi.org/10.1163/156855107780918964

16. Hosoi, A., Arao, Y., Kawada, H.: Transverse crack growth behaviour considering free edge effect in quasi-isotropic cfrp laminates under high-cycle fatigue loading. Compos. Sci. Technol. **69**, 1388–1393 (2009). https://doi.org/10.1016/j.compscitech.2008.09.003

17. Hosoi, A., Shi, J., Sato, N., Kawada, H.: Variations of fatigue damage growth in cross-ply and quasi-isotropic laminates under high-cycle fatigue loading. J. Solid Mech. Mater. Eng. **3**(2), 138–149 (2009). https://doi.org/10.1299/jmmp.3.138

18. Hosoi, A., Sato, N., Kusumoto, Y., Fujiwara, K., Kawada, H.: High-cycle fatigue characteristics of quasi-isotropic cfrp laminates over 10e8 cycles (initiation and propagation of delamination considering interaction with transverse cracks). Int. J. Fatigue **32**, 29–36 (2010). https://doi.org/10.1016/j.ijfatigue.2009.02.028

19. Hosoi, A., Takamura, K., Sato, N., Kawada, H.: Quantitative evaluation of fatigue damage growth in cfrp laminates that changes due to applied stress level. Int. J. Fatigue **33**, 781–787 (2011). https://doi.org/10.1016/j.ijfatigue.2010.12.017

20. Hosoi, A., Sakuma, S., Fujita, Y., Kawada, H.: Prediction of initiation of transverse cracks in cross-ply cfrp laminates under fatigue loading by fatigue properties of unidirectional cfrp in 90 direction. Compos. Part A: Appl. Sci. Manuf. **68**, 398–405 (2015). https://doi.org/10.1016/j.compositesa.2014.10.022

21. Hosoi, A., Kawada, H.: Fatigue life prediction for transverse crack initiation of cfrp cross-ply and quasi-isotropic laminates. Materials (2018). https://doi.org/10.3390/ma11071182

22. Adam, T.J., Horst, P.: Investigation of the very high cycle fatigue behavior of gfrp cross-ply bending specimens. In: Proceedings of the 16th European Conference on Composite Materials, ECCM16, Seville (2014)

23. Adam, T.J., Horst, P.: Experimental investigation of the very high cycle fatigue of GFRP [90/0]s cross-ply specimens subjected to high-frequency four-point bending. Compos. Sci. Technol. **101**, 62–70 (2014). https://doi.org/10.1016/j.compscitech.2014.06.023

24. Adam, T.J.: Ermüdungsverhalten faserverstärkter Kunststoffe im Very-High-Cycle-Fatigue-Bereich. PhD thesis, Technische Universität Braunschweig, Institut für Flugzeugbau und Leichtbau (2016)

25. Adam, T.J., Horst, P.: Very high cycle fatigue of fibre-reinforced composites: an alternative experimental approach. In: Proceedings of the 19th Int. Conference on Composite Materials (2013)

26. Adam, T.J., Horst, P.: Cracking and delamination of cross- and angle-ply gfrp bending specimens under very high cycle fatigue loading. In Proceedings of the 20th Int. Conference on Composite Materials, ICCM20, Copenhagen (2015)

27. Owens Corning. Technical data sheet 111a, 2012. Original document from Owens Corning

28. 3B-fibreglass. Se 2020 datasheet. https://www.3b-fibreglass.com/sites/default/files/products-data-sheets/TDS-SE-2020-DR-for-Epoxy-Resins-2015-sans-trame-LR.pdf, 2015. Original document from 3B-fibreglas

29. Chen, X.: Fabrication and Experimental Material Characterization of RIM135/SE2020 (600Tex). Technische Universität Braunschweig, Institut für Flugzeugbau und Leichtbau, Bachelorarbeit (2019)

30. Richard, H.A., Sander, M.: Ermüdungsrisse: Erkennen, sicher beurteilen, vermeiden. Vieweg+Teubner, Wiesbaden (2009). https://doi.org/10.1007/978-3-8348-9232-4